

Effects of Intrinsic Flame Instabilities on Nitrogen Oxide Formation in Laminar Premixed Ammonia/Hydrogen/Air Flames

Terence Lehmann^{a,*}, Nikita Dimidziev^a, Thomas L. Howarth^a, Michael Gauding^a, Heinz Pitsch^a

^a*Institute for Combustion Technology, RWTH Aachen University, Templergraben 64, 52056 Aachen, Germany*

Abstract

This study investigates the characteristics of nitrogen oxide (NO) formation in two-dimensional (2D) laminar premixed ammonia/hydrogen/air flames and the impact of thermo-diffusively driven intrinsic flame instabilities (IFIs). To this end, a set of three highly resolved direct numerical simulations (DNS) at lean ambient conditions and varying hydrogen fraction in the fuel blend are conducted. The analysis of these DNS reveals a significant increase of NO formation in positively curved regions of the flame, particularly for lower hydrogen fuel fractions, while negatively curved areas exhibit reduced NO concentrations. However, despite the strong variations of local mass fractions of NO in the flame sheet, the mean mass fraction in the post-flame region remains close to the solution from a one-dimensional flame. Through a representative flame segment analysis of positively curved, negatively curved, and flat regions, key reactions contributing to NO formation are determined, with the HNO pathway being the predominant production and the deNO_x pathway being the predominant consumption pathway across all cases. Thermal NO plays no significant role in the considered cases. Generally, the peaks of NO production shift to lower values of progress variable in the negatively curved regions, leading to an annihilation of the production and consumption terms in the low hydrogen fuel fraction case. The decrease of NO production is found to be mainly driven by changes of the radical concentrations, rather than changes of the temperature-dependent reaction rate coefficients.

1. Introduction

The search for adequate replacements of fossil fuels has attracted substantial research efforts, with hydrogen (H₂) and ammonia (NH₃) being identified as two promising candidates [1]. While pure H₂ is difficult to store and transport, and pure NH₃ presents poor combustion properties such as low burning velocities and narrow flammability limits, blends of NH₃/H₂, obtained from partial cracking of NH₃, are a widely considered option for practical use cases [1–3]. However, despite the absence of CO₂ emissions during combustion

*Corresponding author: t.lehmann@itv.rwth-aachen.de

of NH_3/H_2 blends, the formation of nitrogen oxides (NO_x) for such fuels presents a major hindrance for their wide spread application [4–6].

Numerous studies concerning NO_x emission characteristics of premixed NH_3/H_2 flames can be found in the literature. One of the most detailed summaries of nitrogen chemistry was given by Glarborg et al. [7]. Figure 1 depicts a summary of the discussed nitrogen oxide (NO) production and consumption pathways. Here, NH_2 , produced from NH_3 , reacts via HNO, or after a second H-abstraction, via NH to NO. These pathways are referred to as HNO, and NH pathways, respectively. Together, they describe the formation of fuel-NO. In competition with these formation pathways, NO can also be consumed via reactions with NH_2 and NH. These pathways are referred to as de NO_x and N_2O pathways. The Zeldovich mechanism describes the formation of NO via the N radical, which is either produced from NH, or via the so-called thermal pathway $\text{N}_2 + \text{O} = \text{NO} + \text{N}$.

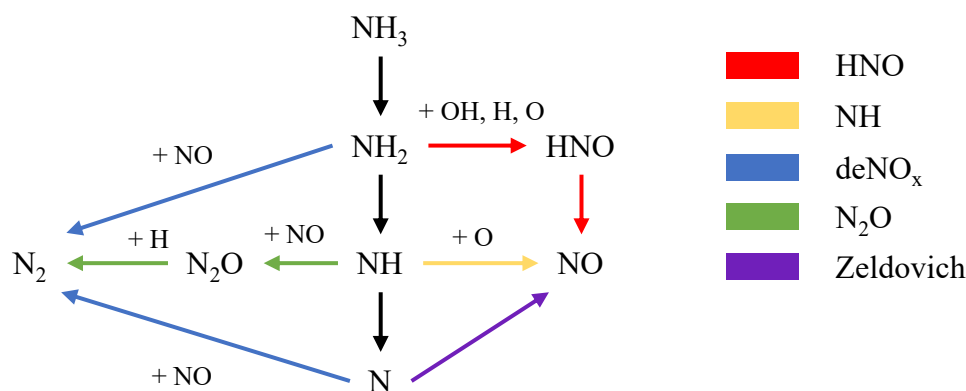


Figure 1: Summary of the most important NO production and consumption pathways for NH_3 combustion following Glarborg et al. [7] and Zhang et al. [8]. For simplicity, some reactions are lumped into a joint pathway for this representation.

Duynslaegher et al. [9] conducted experimental work on planar laminar premixed flames, evaluating flame structure and identifying a profound impact of equivalence ratio ϕ on NO emissions, particularly pronounced for $\phi \in [0.9, 1]$. In their experimental work, Li et al. [10] identified fuel NO as the dominant contributor to NO production over thermal NO for stoichiometric and rich flames, considering different fuel blends ($X_{\text{H}_2,\text{F}} \in [0.33, 0.6]$) and equivalence ratios ($\phi \in \{1, 1.1, 1.25\}$). The molar fraction of H_2 in the H_2/NH_3 fuel blend, is defined as

$$X_{\text{H}_2,\text{F}} = \frac{X_{\text{H}_2}}{X_{\text{H}_2} + X_{\text{NH}_3}}. \quad (1)$$

Nie et al. [11] confirmed the pronounced impact of equivalence ratio on NO formation in NH_3/H_2 flames in their numerical studies for a fuel blend with $X_{\text{H}_2,\text{F}} = 0.3$. Utilizing simulations of shock tubes and laminar premixed counterflow flames, da Rocha et al. [12] compared different reaction mechanisms for the combustion of NH_3/H_2 blends. The authors carried out sensitivity analyses to identify dominant reaction pathways of NO formation.

For a fuel blend with $X_{\text{H}_2,\text{F}} = 0.2$, abundance of O and OH radicals, associated with the fuel-NO pathway, was found to be the main driver of NO emissions. Furthermore, they show that the NO concentrations for pure components, i.e., pure NH_3 or pure H_2 , are lower than those of blends.

By carrying out simulations of one-dimensional (1D) premixed flames for different fuel blends, Zhang et al. [13] employed sensitivity analyses to identify the main contributing reactions for NO formation and consumption. The authors established a relation between NO formation levels and maximum observable OH concentrations, in line with experimental findings by Shi et al. [14]. Higher peak concentrations of OH were linearly correlated with NO formation for equivalence ratios $\phi > 1$. Sensitivity analyses as well as reaction pathway analyses for $\phi = 1.1$ and $X_{\text{H}_2,\text{F}} \in \{0.1, 0.3, 0.5\}$ identified the HNO path associated with fuel-NO as dominant for NO formation. NO consumption was strongly driven by reactions involving amine radicals NH_2 and NH . Furthermore, the importance of the NNH radical for NO consumption was underlined and NO emissions were shown to increase with increasing $X_{\text{H}_2,\text{F}}$.

Several previous studies have demonstrated that NH_3/H_2 blends are susceptible to intrinsic flame instabilities (IFIs) [1, 15]. Netzer et al. [4] studied the impact of artificially induced flame wrinkling on NO production in premixed NH_3/H_2 flames for different equivalence ratios. In agreement with the research mentioned previously, a high spatial correlation between concentrations of OH and NO was found. Local first order correlations showed the NO concentration to be correlated with oxygen mass fraction Y_{O_2} , local equivalence ratio, and the sign of the local curvature. The high diffusivity of H_2 and its consequent impact on the local radical pool in cellular structures caused by flame instabilities was identified as a crucial factor for local NO formation.

Karimkashi et al. [5] investigated the NO_x formation in premixed NH_3/H_2 flames, considering 1D laminar flames for different fuel blends of $X_{\text{H}_2,\text{F}} \in \{0, 0.4, 0.6\}$ as well as one 3D turbulent simulation at $X_{\text{H}_2,\text{F}} = 0.4$ and stoichiometric equivalence ratio. The authors defined different pathways for NO production consisting of sets of elementary reactions and quantified their impact on the net NO formation. For all considered fuel blends in the 1D case, the authors identified the HNO pathway to be the dominant production, and the N_2O pathway to be the dominant consumption route. The impact on the radical pool of H_2 addition was found to significantly affect NO formation, with higher concentrations of H_2 leading to more radical formation and as such a promotion of NO formation through the HNO pathway. Investigations of turbulent flames led the authors to the conclusion that preferential diffusion of H_2 plays a major role in local characteristics of NO formation. Rieth et al. [16] analyzed NO formation in turbulent NH_3/H_2 flames at different equivalence ratios and D’Alessio et al. [17] considered a variation of the pressure.

The present work aims to complement existing research of NO formation in premixed $\text{NH}_3/\text{H}_2/\text{air}$ flames by analyzing the effect of $X_{\text{H}_2,\text{F}}$ in laminar two-dimensional (2D) flames under the influence of IFIs. To this end, three cases with low, medium, and high $X_{\text{H}_2,\text{F}}$ are assessed. This work is structured as follows. First, the numerical methods, models, and the configuration are detailed in the methodology section. Additionally, a method for direct comparison between 1D and 2D simulations, hereafter referred to as flame segment

analysis, is introduced. Next, results for highly resolved 2D direct numerical simulations (DNS) are discussed based on an analysis of global NO_x characteristics as well as a flame segment analysis considering distinct NO formation pathways. The paper closes with the conclusions.

2. Methodology

2.1. Numerical methods and models

The DNS are conducted using PeleLMeX [18, 19]. The code solves the multi-species reactive Navier-Stokes equations within a low-Mach limit [20]. The temporal advancement of these equations is achieved through a spectral-deferred correction method that ensures the conservation of species, mass, and energy [21, 22]. The advection term is discretized using a second-order Godunov scheme. Energy and species equations are treated implicitly with the ODE solver CVODE from the SUNDIALS package [23]. Additionally, PeleLMeX incorporates adaptive mesh refinement (AMR) capabilities inherited from the AMReX package [24], which is used to locally refine the flame front as described below.

Chemical reactions and their associated rates are modeled using the reaction mechanism developed by Zhang et al. [8], which includes 30 species and 243 reactions. This model has shown strong overall performance, demonstrating good quantitative agreement with extensive experimental data regarding flame speed, ignition delay time, and species concentrations [25]. To avoid assumptions related to chemical mechanism reduction, detailed chemistry is utilized. Transport properties are modeled using a mixture-averaged approach including the Soret effect [26]. For details, the reader is referred to Lehmann et al. [15].

2.2. Configuration

2D DNS are carried out in a rectangular domain with dimensions of $L_y = 400l_F$ in streamwise (y) and $L_x = 200l_F$ in crosswise (x) direction. Inflow and outflow conditions are applied at $y = 0$ and $y = 400l_F$, respectively, while a periodic condition is applied in x direction. Here, l_F is the thermal flame thickness defined as $l_F = (T_b - T_u) / (\max(dT/dx))$ in an unstretched premix flame where T denotes the temperature and the indices u and b denote the values in the unburned and burned, respectively. The grid has a base resolution of $n_x \times n_y = 768 \times 1536$ with three levels of AMR leading to a fine resolution of $\Delta x_{\text{Fine}} \approx l_F/30$ within the flame zone. To initialize the simulation, a 1D flamelet computed with FlameMaster [27] is mapped onto the domain and perturbed by a series of $N = 200$ harmonic functions [28], so that the position of the flame is given by

$$y_{\text{Flame}}(x, t = 0) = y_0 + A_0 \sum_{i=1}^N \sin \left(i \frac{2\pi}{L_x} x + \psi(i) \right). \quad (2)$$

Here, $y_0 = 360l_F$ is the initial location of the mean flame front, $A_0 = 0.01l_F$ is the amplitude of each frequency, and $\psi(i) \in [0, 2\pi)$ is a random phase shift obeying a uniform distribution. This initialization equally excites all possibly relevant scales of IFIs and leads to a fast transition to a fully developed statistically steady flame.

Within the scope of this study, three conditions are examined. For all cases, the equivalence ratio is $\phi = 0.6$ at ambient pressure ($p = 1$ bar) and an inlet temperature of $T_u = 298$ K. The molar fraction of H_2 in the fuel blend, as in Eq. (1) is chosen as $X_{H_2,F} \in \{0.4, 0.6, 0.8\}$. These cases will be referred to as low, medium, and high $X_{H_2,F}$ cases hereafter.

2.3. Flame segment construction

To facilitate the comparison between an unstretched 1D reference flame and the local flame state in the 2D, 1D segments are computed from the 2D simulation following the approach of Day et al. [29] and Wen et al. [30]. In contrast to a direct evaluation of the reaction rates on the full domain, the construction of segments allows for a correlation of the pre- and post-flame zone with the local curvature at the flame front. The starting points of the segments are chosen along the isoline of the progress variable based on NH_3 , $C_{NH_3} = 0.95$. The segments are then constructed along the positive and negative gradient of the progress variable C_{H_2O} based on water (H_2O) using a fourth-order Runge-Kutta method and quadratic interpolation with a step size of $\Delta s = 0.1\Delta x_{\text{Fine}}$. The segments are terminated at $C_{H_2O} < 1 \cdot 10^{-2}$ at the lower end, while a minimal gradient of the progress variable criterion of $\Delta C_{H_2O}/\Delta s \leq 1 \cdot 10^{-3}$ is imposed for termination at the upper end. Finally, the species mass fractions are quadratically interpolated onto the segments. Both C_{NH_3} and C_{H_2O} are defined as $C_i = (Y_i - Y_{i,u}) / (Y_{i,b} - Y_{i,u})$. $C_{NH_3} = 0.95$ yields an accurate representation of the peak heat release location and with this the flame geometry, and hence is a suitable choice for the segment's starting points. However, it cannot resolve the NO production zone as NH_3 is fully consumed ($C_{NH_3} = 1$) before the source term of NO approaches zero. On the other hand, C_{H_2O} is unsuitable to represent the flame geometry but exhibits non-zero gradients across the whole NO production zone.

3. Results and discussion

Within this section, the 2D laminar premixed flames are analyzed with respect to NO emissions and compared to a 1D unstretched premixed flame, hereafter referred to as 1D flame. First, the global NO formation characteristics are examined, whereafter a flame segment analysis is conducted.

3.1. NO formation characteristics

Figure 2 shows the distribution of temperature T and NO mass fraction Y_{NO} for $X_{H_2,F} = 0.4, 0.6,$ and 0.8 . From the temperature fields, it becomes evident that in all cases the flame is experiencing thermodiffusive instabilities (TDIs), showing the characteristic flame fingers described in other works [31, 32]. The positively curved regions, i.e., regions where the flame front is convex towards the unburned, show super-adiabatic temperatures with a relative increase of 5.2%, 6.0%, and 5.9% for the low, medium, and high $X_{H_2,F}$ cases, respectively, compared to the 1D flame. In the negatively curved regions, i.e., regions where the flame front is concave towards the unburned, the temperature falls below the adiabatic flame temperature. The low $X_{H_2,F}$ case appears to show the smallest scales of flame structures, which increase with increasing $X_{H_2,F}$.

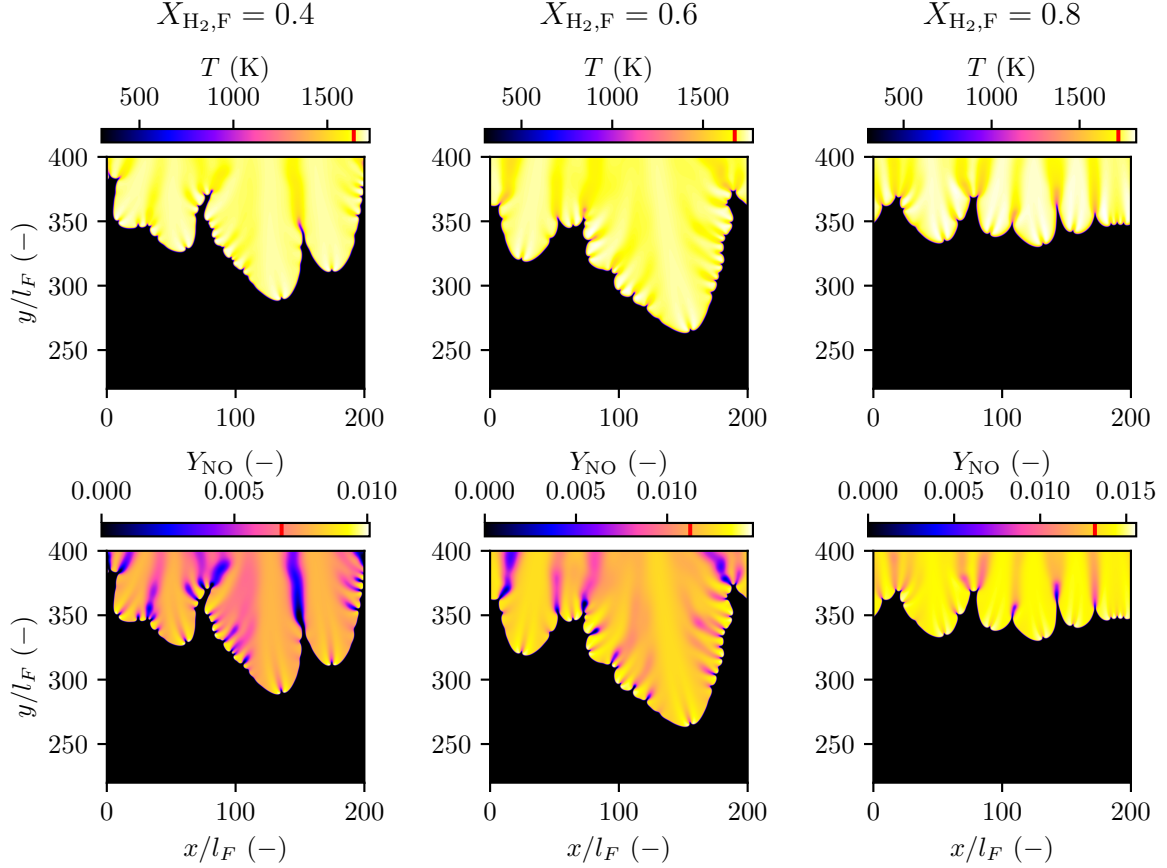


Figure 2: Fields of temperature T (top row) and NO mass fraction Y_{NO} (bottom row) for hydrogen fractions of $X_{\text{H}_2,\text{F}} = 0.4, 0.6, 0.8$ (left to right). Red lines on the color bar represent the burned state in a 1D unstretched premixed flame at the same conditions. Note that the scales are different across the cases to capture their individual details. Conditions: $\phi = 0.6, T_{\text{u}} = 298 \text{ K}, p = 1 \text{ bar}$.

The mass fractions of NO in Fig. 2 generally follow the shape of the flame fingers. Across all cases, Y_{NO} is increased in the positively curved regions compared to the 1D flame. This effect is the strongest for the low $X_{\text{H}_2,\text{F}}$ case with a relative increase of 49%, compared to 31% and 18% in the medium and high $X_{\text{H}_2,\text{F}}$ cases, respectively. At the same time, the high $X_{\text{H}_2,\text{F}}$ case shows the highest absolute values of Y_{NO} in both the 1D and 2D simulation. In the negatively curved regions, Y_{NO} appears to be significantly reduced, showing long trails into the burned region. It is worth mentioning that mass fractions of NO_2 , often considered together with NO as NO_x , is several orders of magnitude lower than that of NO.

Fig. 3 shows the joint probability density functions (jPDFs) of Y_{NO} and $\dot{\omega}_{\text{NO}}$ with $C_{\text{H}_2\text{O}}$. The jPDF between $C_{\text{H}_2\text{O}}$ and Y_{NO} (top row) shows a considerable spread for the low $X_{\text{H}_2,\text{F}}$ case whereas this spread is reduced for the high $X_{\text{H}_2,\text{F}}$ case. More specifically, the jPDF reveals that for low $X_{\text{H}_2,\text{F}}$, regions with $Y_{\text{NO}} \approx 0$ exist for up to $C_{\text{H}_2\text{O}} = 0.8$, whereas this is not the case for the high $X_{\text{H}_2,\text{F}}$ case. A similar behavior is observed for the source term of NO, $\dot{\omega}_{\text{NO}}$ (bottom row), where the relative difference between the 1D flame and the peak

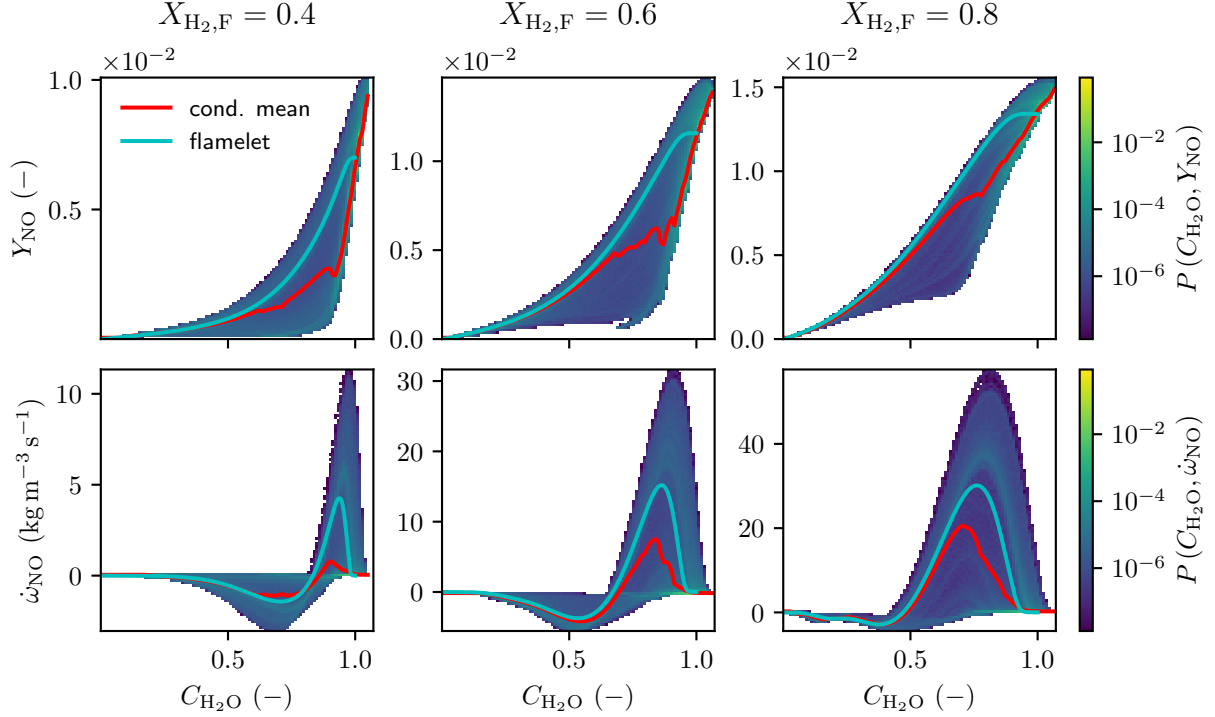


Figure 3: Joint probability density functions (jPDFs) between $C_{\text{H}_2\text{O}}$ and Y_{NO} (top row), $C_{\text{H}_2\text{O}}$ and the source term of NO, $\dot{\omega}_{\text{NO}}$ (bottom row). Red and cyan lines represent the conditional mean and an unstretched 1D profile, respectively. Note that the scales are different across the cases to capture their individual details.

source term in the 2D flame decreases with increasing $X_{\text{H}_2,\text{F}}$. Furthermore, the flamelet as well as the 2D simulation show a region of NO consumption at low progress variable followed by a narrow production zone in the low $X_{\text{H}_2,\text{F}}$ case. This can be explained by the produced NO diffusing upstream, where it is consumed. With increasing $X_{\text{H}_2,\text{F}}$, the production zone is broadened and the consumption zone is flattened.

It is important to notice that for all three cases, the conditional mean of Y_{NO} is lower than the flamelet solution for $C_{\text{H}_2\text{O}} < 1$. Similarly, the conditional mean of $\dot{\omega}_{\text{NO}}$ in the 2D flame shows lower production rates compared the flamelet, especially for the low $X_{\text{H}_2,\text{F}}$ case. Since the values of $C_{\text{H}_2\text{O}}$ do not distinguish the unburnt from the burnt gas region, i.e., can be both greater and smaller than unity, the mean mass fraction of NO in the post flame region defined as

$$\overline{Y_{\text{NO}}^{2\text{D}}} = \frac{m_{\text{NO}}}{m} \Big|_{\text{b}} = \frac{\int_{\Omega_{\text{b}}} \rho Y_{\text{NO}} dV}{\int_{\Omega_{\text{b}}} \rho dV}, \quad (3)$$

is considered to draw conclusions for the exhaust gas composition. Here, m_{NO} and m are the mass of NO and the total gas, respectively, ρ is the density, and Ω_{b} is the burned region downstream of NO production or consumption. However, defining Ω_{b} is not trivial since C_{NH_3} approaches zero within the NO formation regime and $C_{\text{H}_2\text{O}}$ is not bounded. For simplicity, Ω_{b} is thus defined as the area between $y = 395l_{\text{F}}$ and $y = 400l_{\text{F}}$, and Eq. (3) is averaged over multiple timesteps until it converges to a statistically stationary solution.

Since by definition, $\dot{\omega}_{\text{NO}}$ is negligible anywhere within Ω_{b} , the mean mass is constant and consequently \bar{Y}_{NO} does not depend on the exact formulation of the area. Figure 4 shows the results for $\bar{Y}_{\text{NO}}^{2\text{D}}$ along with the exhaust value of 1D flames, $Y_{\text{NO}}^{1\text{D}}$, and the equilibrium NO mass fraction $Y_{\text{NO}}^{\text{eq}}$ over $X_{\text{H}_2,\text{F}}$. Despite the strong increase of local NO mass fractions in the low $X_{\text{H}_2,\text{F}}$ case (Fig. 2), $\bar{Y}_{\text{NO}}^{2\text{D}}$ is 5% smaller than the 1D value, while only an increase of 5% is observed for the high $X_{\text{H}_2,\text{F}}$ case. This effect can be explained by the lower temperature and hence higher density in the negatively curved regions, and consequently their strong impact on $\bar{Y}_{\text{NO}}^{2\text{D}}$. Since Y_{NO} in the negatively curved regions is strongly decreased, this reduces $\bar{Y}_{\text{NO}}^{2\text{D}}$. To further examine the origin in the difference between NO formation in positively and negatively curved regions, a flame segment analysis is carried out in the following section. Finally, it is worth mentioning that $Y_{\text{NO}}^{\text{eq}} < Y_{\text{NO}}^{1\text{D}}$ for most blends. This is related to the partial equilibrium of the fuel-NO pathways results in NO concentrations higher than the global equilibrium. The subsequent decrease to $Y_{\text{NO}}^{\text{eq}}$ is very low, so that no significant gradients are observed.

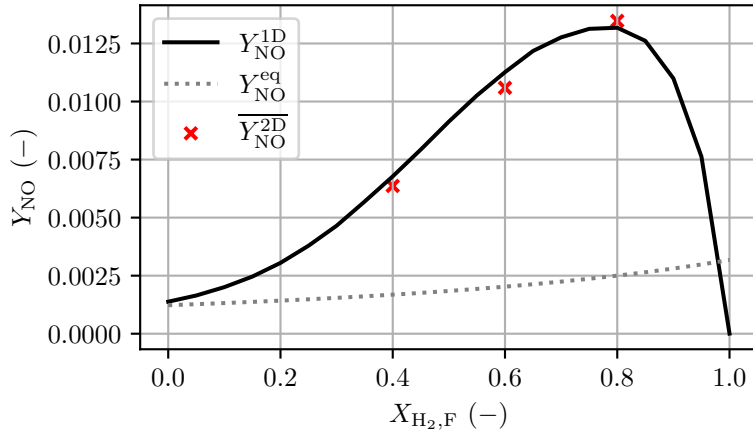


Figure 4: Mass fractions of NO in the equilibrium ($Y_{\text{NO}}^{\text{eq}}$), the burned region of a 1D flame ($Y_{\text{NO}}^{1\text{D}}$), and in the post flame region of a 2D flame as defined in Eq. (3) ($\bar{Y}_{\text{NO}}^{2\text{D}}$) over $X_{\text{H}_2,\text{F}}$.

3.2. Flame segment analysis

One-dimensional flame segments are constructed as outlined in the methodology section, resulting in 22911 segments across the flame for a single timestep. These segments fully cover the flame area relevant to NO consumption and production (see Fig. A.2a in the supplementary material). To assess the impact of local curvature at the flame front on NO production, the segments are then categorized into positive, negative, and neutral curvature segments based on their individual curvature at $C_{\text{NH}_3} = 0.95$. Here, the curvature is defined as divergence of the normal vector of C_{NH_3} which points towards the unburned mixture,

$$\kappa = -\nabla \cdot \frac{\nabla C_{\text{NH}_3}}{|\nabla C_{\text{NH}_3}|}. \quad (4)$$

The threshold is defined as $\kappa \geq \max(\kappa) \cdot 10^{-2}$ for positively curved segments and $\kappa \leq \min(\kappa) \cdot 10^{-2}$ for negatively curved segments. From each of the defined categories, one representative segment is chosen for the following analysis. An assessment of the statistical validity of this procedure is depicted in Fig. A.2b in the supplementary material. As expected from the preceding analysis, the conditional mean $\langle \dot{\omega}_{\text{NO}} | C_{\text{H}_2\text{O}} \rangle$ for the group of segments in the positively and negatively curved regions show a significant difference. While the conditional mean of the segments in positive curvature regions is relatively close to the flamelet solution, they strongly deviate in the negative curvature region. In both cases, the selected representative flame segment lies within one standard deviation from the mean of that curvature range.

Based on the selected segments, the NO formation pathways are analyzed while accounting for the dependence on local curvature. In a first step, the relevant reactions for NO formation are selected from the mechanism with a threshold of 5% contribution to the integrated net NO production or consumption. Following the approach of other studies [5, 16, 17], these reactions are then grouped into the five pathways introduced in Fig. 1, namely the HNO, NH, deNO_x, N₂O, and Zeldovich pathways. A list of the considered reactions and their associated pathway is given in Table A.2 of the supplementary material. Figure 5 shows the production rates $\dot{\omega}_{\text{NO},i}$ for the individual pathways, their sum, and the full mechanism. In all cases, the sum of the pathways, i.e., the production through the subset of selected reactions, aligns well with the production rate calculated based on the full mechanism, indicating that no relevant reactions are neglected. For all cases (flamelet, neutral, positive, and negative curvature), the HNO pathway is dominant for production followed by the NH pathway. The deNO_x pathway is the major consumer of NO followed by the N₂O path. The Zeldovich pathway shows only minor negative to no contribution. These observations are in agreement with Rieth et al. [16]. The production rates of the 1D solution are very similar to the segment from the close-to-zero curvature area. Although the pathways for the segment in the positively curved region show overall higher production rates and are shifted to higher progress variables, their relative importance remains unchanged. For the segment from the negatively curved region, the overall production rates decrease. At the same time, the relative importance of the deNO_x pathway increases. Furthermore, the peaks of the production and consumption pathways align in the $C_{\text{H}_2\text{O}}$ space, leading to a decrease of the net NO formation.

Figure 6 shows the results of the flame segment analysis for the high $X_{\text{H}_2,\text{F}}$ case. An equivalent version of Fig. A.2 for this case is provided in Fig. A.3 in the supplementary material. Similar to the low $X_{\text{H}_2,\text{F}}$ case, the HNO path is the major NO producer, followed by the NH path. Although the deNO_x path shows a decreased importance compared to the low $X_{\text{H}_2,\text{F}}$ case, it still represents the major consumption path. Again, the 1D flame and the segment in the neutrally curved region are very similar. For the positively curved region, the production pathways are enhanced, while the consumption pathways remain at a comparable level as the 1D flame. For the negatively curved region, the relative importance of the deNO_x pathway increases, leading to an overall consumption of NO at lower values of $C_{\text{H}_2\text{O}}$. However, due to the poor alignment of consumption and production regions, high production rates are observed at higher values of progress variable. Compared to the low

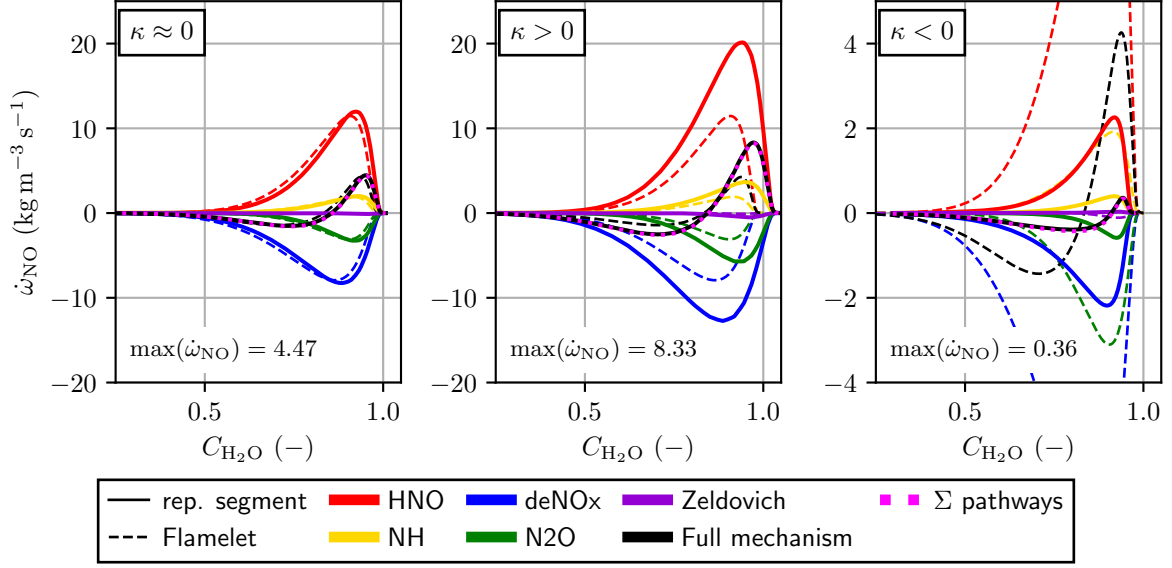


Figure 5: Low $X_{\text{H}_2,\text{F}}$ case: Net production rates $\dot{\omega}_{\text{NO},i}$ for the individual pathways, their sum, and the full mechanism. Top left: Flamelet, top right: neutral curvature, bottom left: positive curvature, bottom right: negative curvature. Note that the y -scale for the bottom right figure is adjusted to capture the details of the individual segments. Conditions: $X_{\text{H}_2,\text{F}} = 0.4$, $\phi = 0.6$, $T_{\text{u}} = 298 \text{ K}$, $p = 1 \text{ bar}$.

$X_{\text{H}_2,\text{F}}$ case, the difference between the total production rate in the positively and negatively curved regions is decreased by a factor of 4. On the macroscopic scale, this leads to the lower spread in Fig. 3 discussed before, and to the overall increase of the mean exhaust mass fraction of NO shown in Fig. 4.

Finally, it remains unclear whether the changes in production rates are an effect of the reduced local temperature or of the changes in local concentrations. In general, the NO production rate of the elementary reaction i can be formulated as

$$\dot{\omega}_{\text{NO},i} = M_{\text{NO}} \nu_{\text{NO},i} \left(k_{i,\text{f}} \prod_{s_j \in \mathcal{S}_i} [s_j]^{\nu'_{s_j}} - k_{i,\text{b}} \prod_{s_j \in \mathcal{S}_i} [s_j]^{\nu''_{s_j}} \right), \quad (5)$$

where M_{NO} is the molar mass of NO, $\nu_{\text{NO},i}$ is the global stoichiometric coefficient of NO in reaction i , and $k_{i,\text{f}}$ and $k_{i,\text{b}}$ are the forward and backward rate coefficients of reaction i , respectively. Further, s_j is a species from the set of species \mathcal{S}_i considered in reaction i , with the concentration $[s_j]$ and the stoichiometric coefficients ν'_{s_j} and ν''_{s_j} in the reactants and products, respectively. Here, $k_{i,\text{f}}$ and $k_{i,\text{b}}$ are dependent on temperature. Figure 7 presents $\dot{\omega}_{\text{NO},i}$ (top row) for the two dominant production and the two dominant consumption reactions, and their decomposition into $[s_j]$ and $k_{i,\text{f}}$ (bottom row) for the flamelet and the segments in positively and negatively curved regions. Note that only forward rates are shown, since the backward reactions are negligible. It becomes evident that the absolute decrease in production rates from positively to negatively curved regions is mostly induced by a change in concentration, since k_i does not show significant changes for the difference

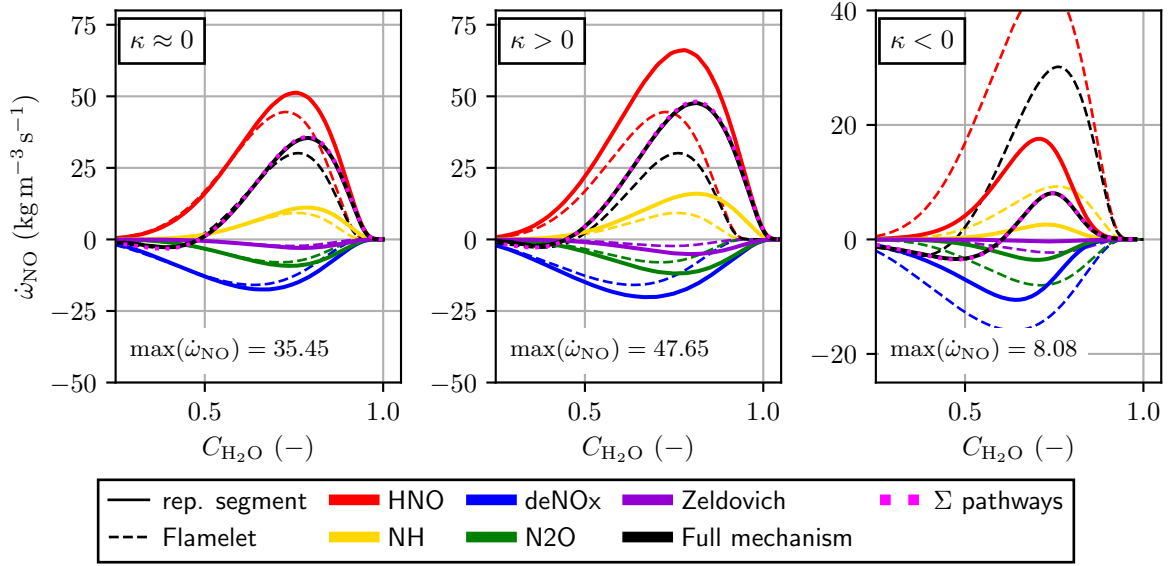


Figure 6: High $X_{\text{H}_2,\text{F}}$ case: Net production rates $\dot{\omega}_{\text{NO},i}$ for the individual pathways, their sum, and the full mechanism. Top left: Flamelet, top right: neutral curvature, bottom left: positive curvature, bottom right: negative curvature. Note that the y -scale for the bottom right figure is adjusted to capture the details of the individual segments. Conditions: $X_{\text{H}_2,\text{F}} = 0.8$, $\phi = 0.6$, $T_{\text{u}} = 298 \text{ K}$, $p = 1 \text{ bar}$.

segments. Especially the H radical shows a significant decrease in concentration for $\kappa < 0$ compared to $\kappa > 0$, most likely related to its high diffusivity.

4. Conclusions

In the presented study, the influence of IFIs on NO formation in laminar premixed $\text{NH}_3/\text{H}_2/\text{air}$ flames under lean, ambient conditions ($\phi = 0.6$, $T_{\text{u}} = 298 \text{ K}$, $p = 1 \text{ bar}$) and varying hydrogen fractions in the fuel blend was analyzed. Across all cases, the influence of IFIs is visible, leading to local temperature overshoots and distinct variations in the NO formation, which, however, are decreasing with increasing $X_{\text{H}_2,\text{F}}$. Although the local mass fraction of NO is increased by up to 49% in the positively curved regions, the mean mass fraction at the outlet is 5% below the exhaust gas values from a 1D unstretched flame. This is related to the strong decrease of NO formation in the negatively curved regions. For the high $X_{\text{H}_2,\text{F}}$ case, the peaks of NO in the positively curved regions, but especially the troughs in the negatively curved regions are less pronounced. This leads to a small relative increase of the mean mass fraction in the post-flame region of the 2D flame compared to the 1D flame.

Next, a flame segment analysis was conducted for the low and high $X_{\text{H}_2,\text{F}}$ cases. The analysis reveals the formation pathway via HNO as the most important, followed by the NH pathway, regardless of $X_{\text{H}_2,\text{F}}$ and the local curvature. Consumption is dominated by the deNO_x pathway followed by the N₂O pathway. Additionally to the absolute changes of NO production rates depending on the local curvature, the relative importance of the deNO_x

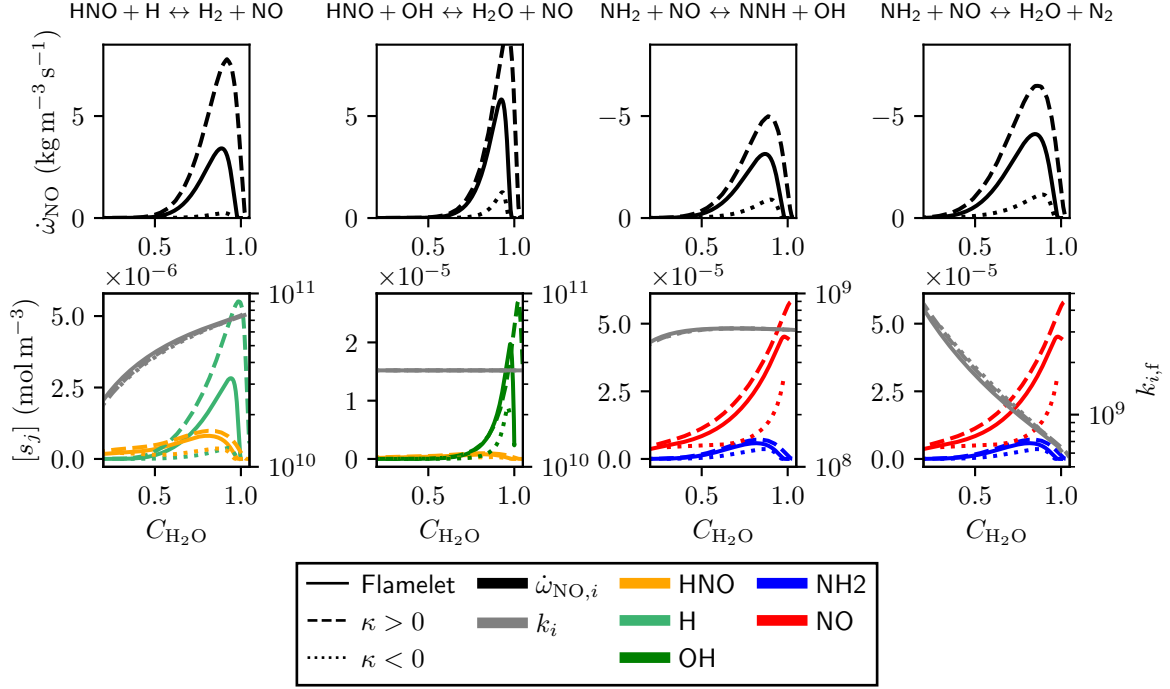


Figure 7: Production rate $\dot{\omega}_{\text{NO},i}$ (top row) and its decomposition into concentration $[s_j]$ (bottom, left axis) and forward reaction rate coefficient $k_{i,f}$ (bottom, right axis) for the two dominant production and consumption reactions. Solid lines represent the value for the 1D reference case, dashed and dotted lines represent values for the positively and negatively curved regions, respectively. Conditions: $X_{\text{H}_2,\text{F}} = 0.4$, $\phi = 0.6$, $T_{\text{u}} = 298 \text{ K}$, $p = 1 \text{ bar}$.

pathway increases in the negatively curved region. Furthermore, in the negatively curved region, production profiles shift to lower values of progress variable. For the low $X_{\text{H}_2,\text{F}}$ case, this leads to an annihilation of production and consumption and hence, lower NO mass fraction. For the high $X_{\text{H}_2,\text{F}}$ case, this annihilation effect is less effective, leading to higher NO mass fraction. Finally, the decrease of NO production is found to be mainly driven by changes of the local radical concentrations, rather than changes of the temperature-dependent reaction rate coefficients.

5. Acknowledgement

TL, ND, MG, and HP gratefully acknowledge the received funding from the European Research Council (ERC) under the European Union’s Horizon 2020 research and innovation program (Grant agreement No. 101054894). TLH acknowledges the generous support by DFG (IRTG 2983 Hy-Potential: Hydrogen - Fundamentals of Production, Storage & Transport, Applications, and Economy).

The authors gratefully acknowledge the computing time provided to them at the NHR Center NHR4CES at RWTH Aachen University (project numbers p0020340 and p0020410). This is funded by the Federal Ministry of Education and Research, and the state governments

participating on the basis of the resolutions of the GWK for national high performance computing at universities (www.nhr-verein.de/unsere-partner).

References

- [1] Kobayashi, H., Hayakawa, A., Somarathne, K.D.K.A., Okafor, E.C., “Science and technology of ammonia combustion”, *Proc. Combust. Inst.* 37(1): 109–133 (2019).
- [2] Elbaz, A.M., Wang, S., Guiberti, T.F., Roberts, W.L., “Review on the recent advances on ammonia combustion from the fundamentals to the applications”, *Fuel Communications* 10: 100053 (2022).
- [3] Valera-Medina, A., Xiao, H., Owen-Jones, M., David, W.I.F., Bowen, P.J., “Ammonia for power”, *Prog. Energy Combust.* 69: 63–102 (2018).
- [4] Netzer, C., Ahmed, A., Gruber, A., Løvås, T., “Curvature effects on NO formation in wrinkled laminar ammonia/hydrogen/nitrogen-air premixed flames”, *Combust. Flame* 232 (2021).
- [5] Karimkashi, S., Tamadonfar, P., Kaario, O., Vuorinen, V., “A numerical investigation on effects of hydrogen enrichment and turbulence on NO formation pathways in premixed ammonia/air flames”, *Combust. Sci. Technol.* (2023).
- [6] Awad, O.I., Zhou, B., Harrath, K., Kadirgama, K., “Characteristics of NH₃/H₂ blend as carbon-free fuels: A review”, *Int. J. Hydrogen Energy.* 48: 38077–38100 (2023).
- [7] Glarborg, P., Miller, J.A., Ruscic, B., Klippenstein, S.J., “Modeling nitrogen chemistry in combustion”, *Prog. Energy Combust. Sci.* 67: 31–68 (2018).
- [8] Zhang, X.Y., Moosakutty, S.P., Rajan, R.P., Younes, M., Sarathy, S.M., “Combustion chemistry of ammonia/hydrogen mixtures: Jet-stirred reactor measurements and comprehensive kinetic modeling”, *Combust. Flame* 234: 111653 (2021).
- [9] Duynslaegher, C., Jeanmart, H., Vandooren, J., “Flame structure studies of premixed ammonia/hydrogen/oxygen/argon flames: Experimental and numerical investigation”, *Proc. Combust. Inst.* 32 I: 1277–1284 (2009).
- [10] Li, J., Huang, H., Kobayashi, N., He, Z., Nagai, Y., “Study on using hydrogen and ammonia as fuels: Combustion characteristics and NO_x formation”, *Int. J. Energy Res.* 38: 1214–1223 (2014).
- [11] Nie, T., Zhang, P., Yang, K., Zhou, L., Zheng, X., Luo, L., “Study on laminar combustion characteristics of ammonia/ hydrogen premixed based on chemical reaction kinetics”, vol. 406, EDP Sciences (2023).
- [12] da Rocha, R.C., Costa, M., Bai, X.S., “Chemical kinetic modelling of ammonia/hydrogen/air ignition, premixed flame propagation and NO emission”, *Fuel* 246: 24–33 (2019).
- [13] Zhang, J., Huang, M., Tang, B., Liu, Z., Zhang, H., Song, Y., Fan, X., Sha, H., Niu, X., “The impact of hydrogen addition and OH concentration on NO emissions in high-pressure NH₃/air combustion”, *Int. J. Hydrogen Energy.* 54: 1017–1028 (2024).
- [14] Shi, H., Liu, S., Zou, C., Dai, L., Li, J., Xia, W., Yang, J., Luo, J., Li, W., “Experimental study and mechanism analysis of the NO_x emissions in the NH₃ mild combustion by a novel burner”, *Fuel* 310: 122417 (2022).
- [15] Lehmann, T., Berger, L., Howarth, T.L., Gauding, M., Girhe, S., Dally, B.B., Pitsch, H., “Comprehensive linear stability analysis for intrinsic instabilities in premixed ammonia/hydrogen/air flames”, arXiv:2410.11466 [physics.flu-dyn] (2024).
- [16] Rieth, M., Gruber, A., Chen, J.H., “A direct numerical simulation study on NO and N₂O formation in turbulent premixed ammonia/hydrogen/nitrogen-air flames”, *Proc. Combust. Inst.* 39(2): 2279–2288 (2023).
- [17] D’Alessio, F., Lapenna, P.E., Bottari, S., Creta, F., “Intrinsically unstable hydrogen-enriched premixed ammonia flames: Analysis and modeling of NO formation”, *Proc. Combust. Inst.* 40(1): 105485 (2024).
- [18] Esclapez, L., Day, M., Bell, J., Felden, A., Gilet, C., Grout, R., Henry de Frahan, M., Motheau, E., Nonaka, A., Owen, L., Perry, B., Rood, J., Wimer, N., Zhang, W., “PeleLMEx: an AMR Low Mach Number Reactive Flow Simulation Code without level sub-cycling”, *J. Open Source Softw.* 8(90): 5450 (2023).

- [19] Henry de Frahan, M.T., Esclapez, L., Rood, J., Wimer, N.T., Mullaney, P., Perry, B.A., Owen, L., Sitaraman, H., Yellapantula, S., Hassanaly, M., Rahimi, M.J., Martin, M.J., Doronina, O.A., A., S.N., Rieth, M., Ge, W., Sankaran, R., Almgren, A.S., Zhang, W., Bell, J.B., Grout, R., Day, M.S., Chen, J.H., “The Pele simulation suite for reacting flows at exascale”, *Proceedings of the 2024 SIAM Conference on Parallel Processing for Scientific Computing* pp. 13–25 (2024).
- [20] Day, M.S., Bell, J.B., “Numerical simulation of laminar reacting flows with complex chemistry”, *Combust. Theor. Model.* 4(4): 535 (2000).
- [21] Nonaka, A., Bell, J., Day, M., Gilet, C., Almgren, A., Minion, M., “A deferred correction coupling strategy for low Mach number flow with complex chemistry”, *Combust. Theor. Model.* 16(6): 1053–1088 (2012).
- [22] Nonaka, A., Day, M.S., Bell, J.B., “A conservative, thermodynamically consistent numerical approach for low Mach number combustion. Part I: single-level integration”, *Combust. Theor. Model.* 22(1): 156–184 (2018).
- [23] Hindmarsh, A.C., Brown, P.N., Grant, K.E., Lee, S.L., Serban, R., Shumaker, D.E., Woodward, C.S., “SUNDIALS: Suite of nonlinear and differential/algebraic equation solvers”, *ACM T. Math. Software* 31(3): 363–396 (2005).
- [24] Zhang, W., Almgren, A., Beckner, V., Bell, J., Blaschke, J., Chan, C., Day, M., Friesen, B., Gott, K., Graves, D., Katz, M., Myers, A., Nguyen, T., Nonaka, A., Rosso, M., Williams, S., Zingale, M., “AMReX: a framework for block-structured adaptive mesh refinement”, *J. Open Source Softw.* 4(37): 1370 (2019).
- [25] Girhe, S., Snackers, A., Lehmann, T., Langer, R., Loffredo, F., Glaznev, R., Beeckmann, J., Pitsch, H., “Ammonia and ammonia/hydrogen combustion: Comprehensive quantitative assessment of kinetic models and examination of critical parameters”, *Combust. Flame* 267: 113560 (2024).
- [26] Howarth, T.L., Day, M.S., Pitsch, H., Aspden, A.J., “Thermal diffusion, exhaust gas recirculation and blending effects on lean premixed hydrogen flames”, *Proc. Combust. Inst.* 40(1): 105429 (2024).
- [27] Pitsch, H., “FlameMaster: A C++ computer program for 0D combustion and 1D laminar flame calculations”, (1998).
- [28] Al Kassar, S., Berger, L., Lapenna, P.E., Creta, F., Pitsch, H., Attili, A., “Efficient and accurate calculation of dispersion relations for intrinsically unstable premixed flames”, *Combust. Flame* 269: 113640 (2024).
- [29] Day, M., Bell, J., Bremer, P.T., Pascucci, V., Beckner, V., Lijewski, M., “Turbulence effects on cellular burning structures in lean premixed hydrogen flames”, *Combust. Flame* 156(5): 1035–1045 (2009).
- [30] Wen, X., Berger, L., vom Lehn, F., Parente, A., Pitsch, H., “Numerical analysis and flamelet modeling of NOx formation in a thermodynamically unstable hydrogen flame”, *Combust. Flame* 253: 112817 (2023).
- [31] Berger, L., Kleinheinz, K., Attili, A., Pitsch, H., “Characteristic patterns of thermodynamically unstable premixed lean hydrogen flames”, *Proc. Combust. Inst.* 37(2): 1879–1886 (2019).
- [32] Howarth, T.L., Aspden, A.J., “An empirical characteristic scaling model for freely-propagating lean premixed hydrogen flames”, *Combust. Flame* 237 (2022).

6. Supplementary material

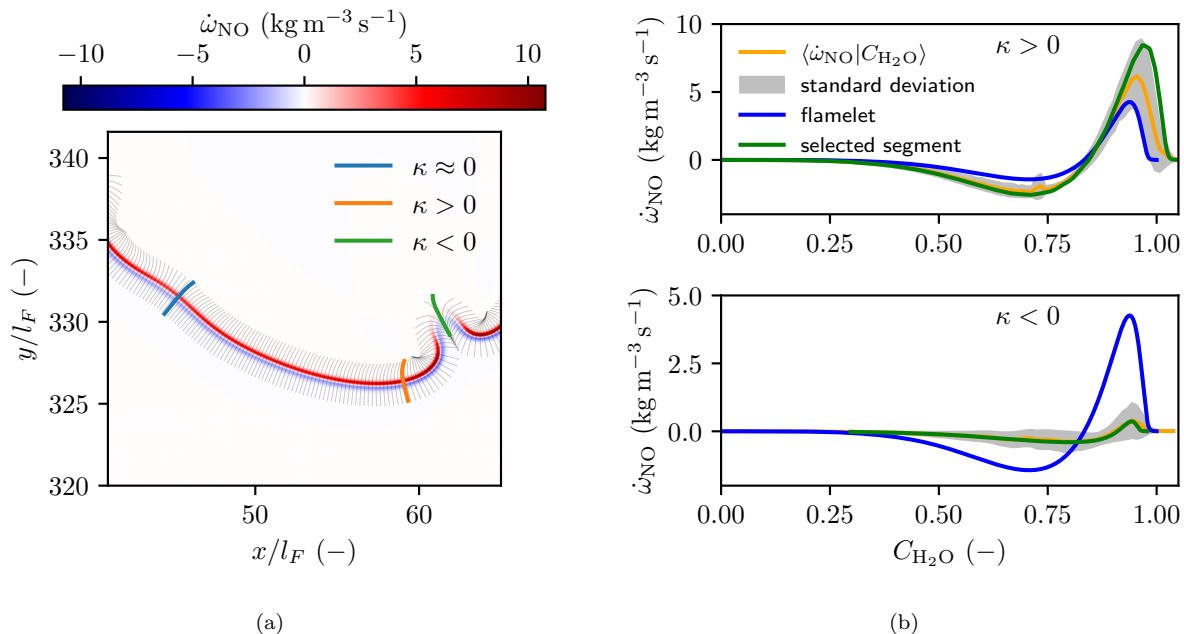
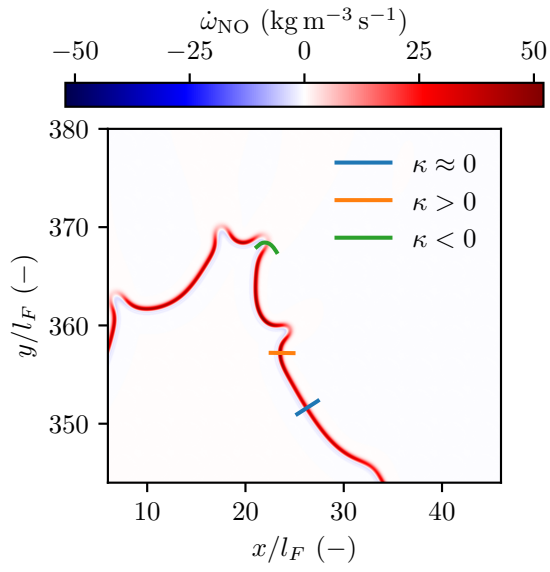


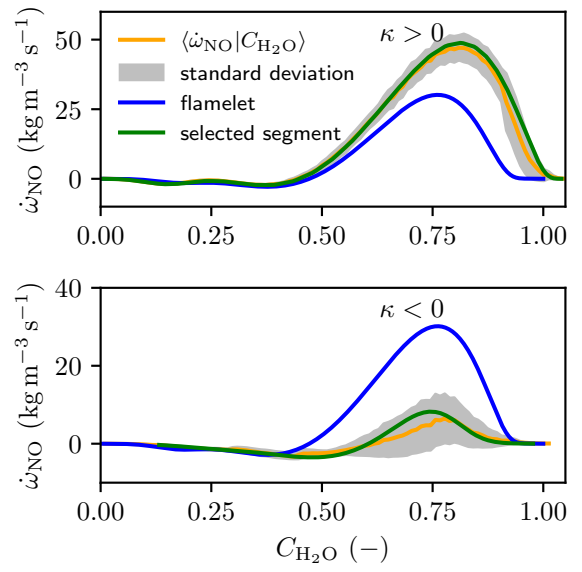
Figure A.2: Assessment of the statistical validity of the segment selection procedure. (a) Constructed segments (thin gray lines) on the spatial distribution of the NO production term $\dot{\omega}_{\text{NO}}$. The path density is reduced by a factor of 10 for visualization purposes. Thick colored lines depict the selected representative segments. (b) Mean of $\dot{\omega}_{\text{NO}}$ conditioned on $C_{\text{H}_2\text{O}}$, its standard deviation within the category, the 1D reference flame, and the selected representative segment for the group of positive (top) and negative (bottom) curved segments. Note that the scales in (b) are different across the two categories to capture their individual details. Conditions: $X_{\text{H}_2, \text{F}} = 0.4$, $\phi = 0.6$, $T_{\text{u}} = 298 \text{ K}$, $p = 1 \text{ bar}$.

Table A.2: NO reactions incorporated in this study, grouped by their associated pathways.

Reaction no.	Chemical Formulation	Pathway
69	$\text{NH}_2 + \text{HNO} \rightleftharpoons \text{NH}_3 + \text{NO}$	HNO
173	$\text{HNO} \rightleftharpoons \text{NO} + \text{H}$	
174	$\text{HNO} + \text{O} \rightleftharpoons \text{NO} + \text{OH}$	
175	$\text{HNO} + \text{H} \rightleftharpoons \text{NO} + \text{H}_2$	
176	$\text{HNO} + \text{OH} \rightleftharpoons \text{NO} + \text{H}_2\text{O}$	
177	$\text{HNO} + \text{O}_2 \rightleftharpoons \text{NO} + \text{HO}_2$	
180	$\text{HNO} + \text{NH} \rightleftharpoons \text{NH}_2 + \text{NO}$	
38	$\text{NH} + \text{O} \rightleftharpoons \text{NO} + \text{H}$	NH
43	$\text{NH} + \text{O}_2 \rightleftharpoons \text{NO} + \text{OH}$	
48	$\text{NH} + \text{NO} \rightleftharpoons \text{N}_2 + \text{OH}$	deNO _x
64	$\text{NH}_2 + \text{NO} \rightleftharpoons \text{NNH} + \text{OH}$	
65/66	$\text{NH}_2 + \text{NO} \rightleftharpoons \text{N}_2 + \text{H}_2\text{O}$	
47	$\text{NH} + \text{NO} \rightleftharpoons \text{N}_2\text{O} + \text{H}$	N ₂ O
79	$\text{N}_2\text{H}_2 + \text{NO} \rightleftharpoons \text{N}_2\text{O} + \text{NH}_2$	
34	$\text{N} + \text{O}_2 \rightleftharpoons \text{NO} + \text{O}$	Zeldovich
35	$\text{N} + \text{OH} \rightleftharpoons \text{NO} + \text{H}$	
36	$\text{N} + \text{NO} \rightleftharpoons \text{N}_2 + \text{O}$	



(a)



(b)

Figure A.3: Assessment of the statistical validity of the segment selection procedure. (a) Selected representative segments on the spatial distribution of the NO production term $\dot{\omega}_{\text{NO}}$. (b) Mean of $\dot{\omega}_{\text{NO}}$ conditioned on $C_{\text{H}_2\text{O}}$, its standard deviation within the category, the 1D reference flame, and the selected representative segment for the group of positive (top) and negative (bottom) curved segments. Note that the scales in (b) are different across the two categories to capture their individual details. Conditions: $X_{\text{H}_2, \text{F}} = 0.8$, $\phi = 0.6$, $T_{\text{u}} = 298 \text{ K}$, $p = 1 \text{ bar}$.